Effect of Mixer Geometry and Operating Conditions on Flow Mixing of Shear Thinning Fluids with Yield Stress

Jaime Sossa-Echeverria and Fariborz Taghipour
Chemical and Biological Engineering Dept., University of British Columbia,
2360 East Mall, Vancouver, BC, V6T 1Z3, Canada

DOI 10.1002/aic.14309
Published online December 27, 2013 in Wiley Online Library (wileyonlinelibrary.com)

Flow mixing of a non-Newtonian fluid in a stirred tank equipped with a side-entry impeller was observed using particle image velocimetry (PIV). The effects of some geometrical parameters including the mixer shape and impeller type and position on the flow pattern were studied on velocity fields obtained at different locations inside the mixing domain. The different flow structures revealed that the ratio of inertial and viscous forces largely defines the flow pattern. Dead zones were observed inside the tank due to the rheological properties of the fluid. The size of the dynamic regions and the average velocity near the impeller were enhanced by increasing the suction area. Likewise, large pitch ratios were found to improve the active mixing zone and the axial discharge. Curves for the power and pumping numbers are reported for different axial flow impellers. © 2013 American Institute of Chemical Engineers *AIChE J*, 60: 1156–1167, 2014
Keywords: fluid mechanics, mixing

Introduction

Mechanically stirred vessels play an important role in the production chain of a wide range of industrial processes. Their design and optimization require a fundamental understanding of all the variables potentially affecting the performance of these essential units. Some of these variables include geometrical parameters that are characteristic of the mixing equipment, such as vessel shape, impeller geometry, baffles, number of impellers and impeller clearance. The existing diversity of each of these parameters provides an enormous spectrum of possibilities to tackle any mixing necessity.

Previous studies have shown the effect of impeller design on mixing flow under different operating conditions. Axial flow impellers are characterized by both axial and radial flow discharge in the case of low to medium viscosities. Kelly and Gigas[1] have shown that this discharge angle is strongly related to the Reynolds number in the laminar and transitional flow regimes.

Geometrical characteristics of an impeller, to a great degree determine its performance. The pitch is defined as the distance a point on an impeller blade would move along the axis of rotation in one revolution of the impeller. A positive correlation has been determined between pitch ratio (ratio of the pitch to the impeller diameter) and other impeller properties like power number (N_p), axial force number (N_f), and pumping number (N_q) for axial flow impellers.[2,3] Definitions for these impeller properties are presented in Eqs. 1–3. The use of the prefactors in Eqs. 1–3 is to adjust the selected unit inputs

$$N_p = 1 \times 10^{10} \frac{P}{\rho N^3 D^5} \tag{1}$$

$$N_f = 1 \times 10^{8} \frac{F_A}{\rho N^2 D^4} \tag{2}$$

$$N_q = 1 \times 10^{6} \frac{Q}{N D^3} \tag{3}$$

The power number can be reduced by keeping a nearly constant pitch across the blade, i.e., using hydrofoil impellers.[4] The hydrofoil impellers offer axial flow with lower shear compared to conventional axial flow impellers. The nearly constant pitch across the blade of hydrofoil impellers provides a more uniform velocity distribution in the discharge area, which is suitable for applications where high-shear rates can harm the fluid. Another important parameter, affecting power consumption and flow pattern is the impeller location. There are some guidelines in literature for impeller clearance (distance between the impeller and vessel rear wall) based on empirical work.[5,6] However, their applicability might be limited to specific conditions, since the optimum dimensionless clearance E/D (where E is the clearance from rear-wall, and D is the impeller diameter) is a function of operating conditions, rheology, and mechanical constraints. Bhole et al.[6] used electrical resistance tomography to identify dead zones inside a stock chest and showed that for a 3% hardwood pulp suspension the optimal E/D ratio is close to 0.5. Moreover, they found a substantial restriction of the flow to the impeller suction at E/D = 0.14, which leads to an increase of the power requirements.

Besides impeller characteristics and location, the vessel shape can be a key variable when designing mixing systems. The most common configuration for stirred tanks is the

Correspondence concerning this article should be addressed to F. Taghipour at fariborz@chbe.ubc.ca.

cylindrical vessel equipped with top entry impellers, performance of which is well described in literature. Other nonconventional arrangements are cylindrical and rectangular vessels equipped with side entry impellers. These systems are used in industrial processes such as wastewater treatment and agitation of pulp fiber suspensions among others. Gomez et al.[7] reported characteristic flow structures of a viscous Newtonian fluid in a rectangular vessel equipped with a side entry impeller. This study revealed the radial discharge of an axial flow impeller due to high viscosity of the fluid, and showed the evolution of the flow for different Reynolds numbers.

Different techniques are applied to study mixing dynamics. Particle image velocimetry (PIV) is a powerful experimental technique to obtain meaningful data about the flow field at specific positions inside the mixing domain. Unlike other nonintrusive visualization techniques like particle tracking velocimetry (PTV) and laser doppler velocimetry (LDV), PIV provides high-density velocity fields in a defined grid, which may reveal circulation flow patterns and velocity gradients.[8] This technique extracts instantaneous local velocities of the fluid by measuring the displacement of small tracer particles in a known time interval. A detail explanation of this technique can be found in Adrian,[8] Prasad[9] and Mckenna and Mcgillis.[10]

PIV is an optically-based visualization technique and its implementation demands the use of transparent fluids so that the tracer particles can be seen through the flow. Aqueous Carbopol solutions are transparent fluids, which are also able to mimic complex rheological behavior of some industrial fluids. Those properties make Carbopol solutions suitable for the development of this work. Some studies have shown the rheological properties of Carbopol solutions and their similarities with complex fluids found in industrial processes.[11,12] A Carbopol solution is a water-swellable microgel,[13] composed of highly crosslinked polymer chains and generally speaking, it exhibits shear-thinning behavior with yield stress.[14] Although the concept of yield stress is controversial, it has been shown that it provides an appropriate way to describe the macroscale flow conditions under different shear rate values. Gomez et al.[15] presented qualitative similarities of aqueous Carbopol solutions and pulp suspensions, along with a set of conditions to mimic the mixing quality attained in a particular pulp suspension mixing system. Several studies of mixing of non-Newtonian fluids with yield stress show strong segregation, i.e., an active zone around the impeller (known as cavern) and a stagnant zone away from the impeller. The relation between the cavern geometry (size and shape) and the fluid dynamics inside are not fully understood. Its prediction can be challenging, since both are strongly related to the specific conditions of each mixing system.

Most of the studies describing flow structures inside stirred tanks are focused on vessels equipped with top entry impellers. However, mixing vessels with side entry impellers are also valuable alternatives, since those provide asymmetric flow, smaller shaft lengths (for tall tanks) and lower initial cost.[4,6] These specifications make them very popular for special industrial processes such as mixing of pulp fibers and sludge control in oil tanks. Hence, this study was meant to investigate the flow structures generated in stirred tanks equipped with side entry impellers. The hydrodynamics of a non-Newtonian fluid with yield stress was studied for different impeller shapes, clearances and vessel shapes.

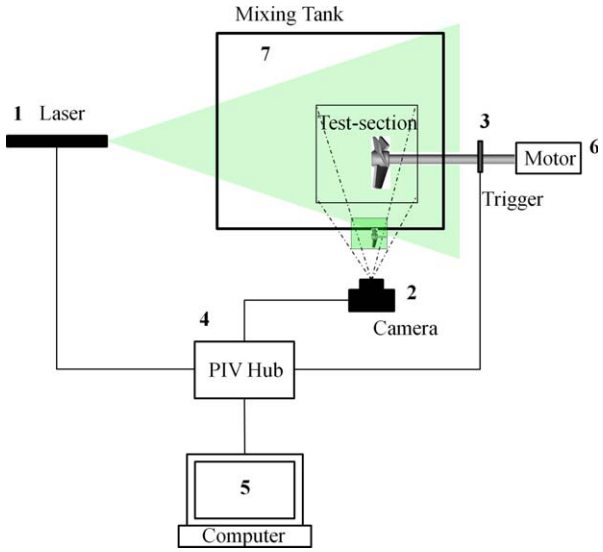

Figure 1. PIV experimental setup.

[Color figure can be viewed in the online issue, which is available at wileyonlinelibrary.com.]

Experiments

Experimental setup

A 2D-PIV system from Dantec Dynamics, Inc., was used for measuring the flow field. The basic components of the experimental setup are presented in Figure 1. The system consists of (1) a dual head Nd:YAG laser to illuminate the region of interest, (2) a high-resolution (1344 $\times$ 1024 pixels) progressive-scan interline CCD camera (Hamamatsu, model HiSense MkII) to record the position of the tracer particles at two successive snapshots, (3) a triggering system composed of a proximity switch (Wenglor IB40) and an aluminum rod mounted on the impeller shaft (this system activates the photoacquisition system at specific positions of the impeller), (4) a PIV hub that controls the time between laser pulses and synchronizes the action of the trigger with the laser and the camera, (5) a personal computer that operates the PIV hub, stores photos and obtains velocity fields from cross-correlation techniques, (6) a 0.33 HP motor with a digital control of the motor speed, and (7) a transparent Plexiglas mixing tank of approximately 0.03 m^3 containing the fluid which is uniformly seeded with tracer particles that are neutrally buoyant. These are polymer particles (size distribution of 20–50 μm and density of 1,100 kg/m^3) with a fluorescent dye (Rhodamine B) uniformly distributed over the particle volume. Rhodamine B has been previously used as tracer dye in planar laser induced fluorescence (PLIF) experiments.[16,17] The seeding material was chosen to not alter fluid or flow properties. Particle size and shape, specific gravity and surface characteristics are chosen to keep the Stokes number at very low values. A trade-off between flow tracking and light scattering is required when choosing particle size.

Two tanks of cylindrical and rectangular shapes, with similar volumetric capacity were used. The dimensions of the cylindrical tank (Figure 2a) are diameter $T = 32.9$ cm and height $H = 35$ cm, whereas for the rectangular tank (Figure 2b) they are length $l = 36.5$ cm, width $W = 24.5$ cm, and height $H = 35$ cm. As shown in Figure 2a and 2b, three different vertical planes (test-sections) inside the tanks were

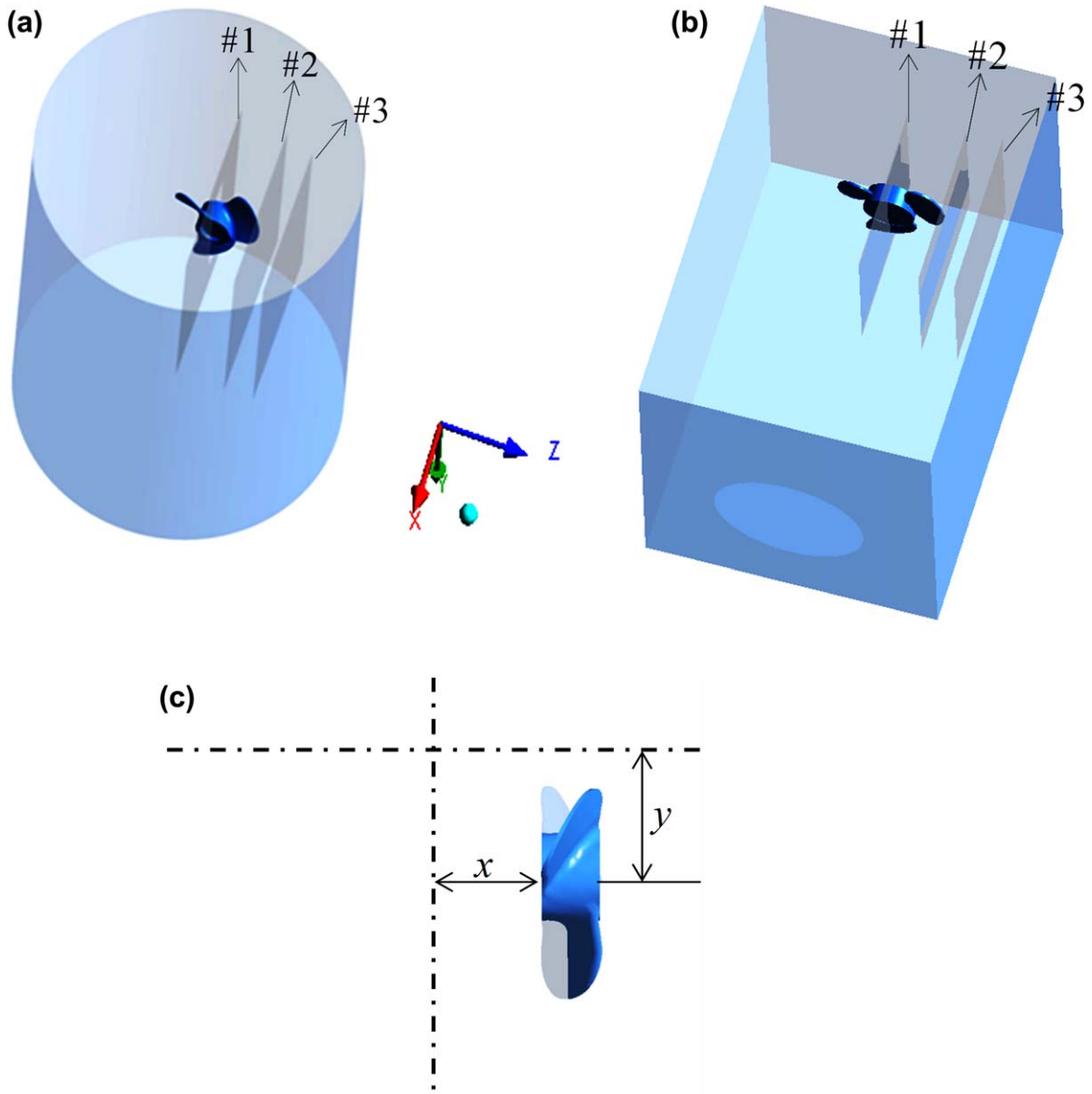

Figure 2. Mixing tanks and test sections (a) cylindrical tank, (b) rectangular tank, and (c) test section and sample lines for velocity profiles.

[Color figure can be viewed in the online issue, which is available at wileyonlinelibrary.com.]

investigated, that is, one (#1) at the center of the impeller ($Z = 0$ cm), another (#2) close to the blade tip ($Z = 5$ cm) and one (#3) close to the tank wall ($Z = 8$ cm). These planes are generated by aligning the light sheet created by the laser (with a thickness of approximately 2 mm) with the sought "Z" position and by framing, with the camera, the desired area around the impeller. The light refracted by the plane was filtered using a 570 nm filter at the camera lens, so that the light beams refracted by air bubbles was not recorded and only those from the particles were captured.

The flow field of three impellers (Figure 3) with diameter D = 9.652 cm was studied. These are three bladed, axial-flow hydrofoil impellers used at industrial level, in mixers with side-entry impellers. One of the main differences among the three impellers is the pitch ratio ranging from low to high, i.e., 0.44, 0.9 and 1.5 at the blade tip for the Maxflo Mark II, A312 and A100 impellers, respectively. The distance from the bottom wall was kept constant at 7.4 cm throughout the experiments. The flow field was evaluated at four different impeller clearances from the side wall ($E/D = 0.26$, 0.56, 0.62, and 0.72). This range covers E/D ratios used in other studies.[5,6]

Model fluid and rheology

The model fluid for this study was an aqueous Carbopol solution ($\rho = 1085$ kg/m^3), with a concentration of 0.09 w/wt % of Carbopol 940 (Noveon, Inc.). Rheological properties of industrial fluids can be imitated using similar Carbopol concentrations as shown by Gomez et al.[15] The solution was prepared through hydration of the polymer with deionized water followed by a neutralization process to increase the pH to 7. The neutralization was done using an 18% NaOH solution (2.3 parts of NaOH solution per part of polymer by weight). A more complete description of the preparation process can be found at Gomez et al.[15] The initial solution was neutralized to promote the formation of microgel particles

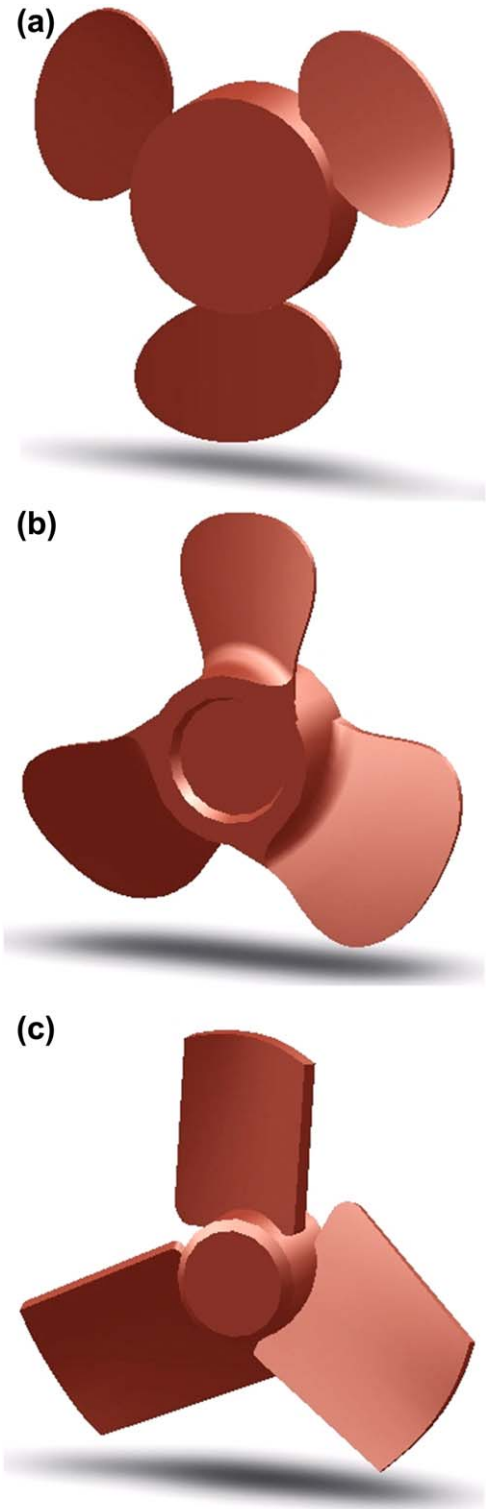

Figure 3. Axial flow impellers (a) Maxflo Mark II impeller, (b) A100 impeller, and (c) A312 impeller.

[Color figure can be viewed in the online issue, which is available at wileyonlinelibrary.com.]

and enhance the formation of hydrogen bonds between the particles and water; thereby the solution becomes thicker and exhibits an apparent yield stress.[11,18] The definition of yield stress and even its existence in fluid rheology may be controversial, but a practical definition is the stress at which significant flow occurs (shear rate $\dot{\gamma} \cong 0$). The yield stress of the Carbopol solution was measured using a vane in a DV-III Ultra Rheometer from Brookfield. The resistance of the material to flow is measured by tracking the increments of imparted torque as the motor rotates at low rotational speed (3.33×10^{-4} s^{-1}). The standard deviation of four measurements of yield stress under different rotational speeds was found to be 0.57 Pa. The torque is measured at specific time intervals and the yield stress value is derived from the maximum torque (Figure 4). The sample was presheared at 8.3×10^{-3} s^{-1} for 100 s and let to stand for 100 s before running the experiment. Consecutive test with different Carbopol samples resulted in a yield stress of 10.8 ± 0.8 Pa (95% confidence interval).

The rheological characterization at stresses higher than the yield stress was obtained with a controlled rate rheometer (DV-III Ultra), using vane and wide-gap cup geometry. The shear rate and shear stress were computed from Eqs. 4 and 5, respectively

$$\dot{\gamma}_b = 2\Omega \frac{dln\Omega}{dln\tau_b} \tag{4}$$

$$\tau = \frac{M}{2\pi R_b{}^2 L_b} \tag{5}$$

These equations were derived by treating the vane geometry as a cylinder of fluid with the same diameter as the vane.[19,20] Equation 5 can be applied if the no-slip boundary condition is valid.[20] To obtain rheological data relevant at the operating conditions used in this research, it was necessary to roughly estimate an average shear rate inside the cavern. A first approximation of the existing shear rates in the mixing system was obtained using an expression derived by Metzner and Otto[21] that relates shear rate and impeller speed (N) by a constant value K_s ($\dot{\gamma} = K_s N$). Although it has been shown that this relationship is inaccurate for some systems, it has been effectively implemented at low Reynolds numbers.[22] For the impellers and rotational speeds used in this research the highest shear rate was 125 s^{-1} with a $K_s = 11$[23] and $N = 11.4$ s^{-1} (maximum angular speed). The angular speeds were selected in order to cover a wide range of operating conditions in the laminar and transitional flow regimes. Thus, the highest angular speed was selected to be close to the turbulent regime. On the other hand, the yield stress of the Carbopol solutions dictates the minimum required velocity to create a meaningful cavern volume.

Figure 5 presents the rheological characterization of a 0.09 w/wt % Carbopol solution. The constant slope below 40 s^{-1} in Figure 5 reflects the shear thinning behavior of the Carbopol solution. Considering the yield stress, the

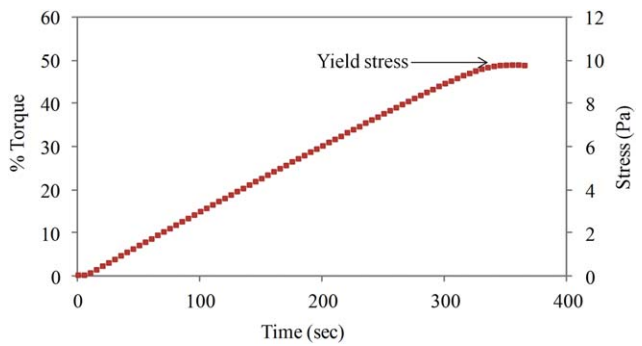

Figure 4. Yield stress of 0.09 wt% Carbopol solution.

[Color figure can be viewed in the online issue, which is available at wileyonlinelibrary.com.]

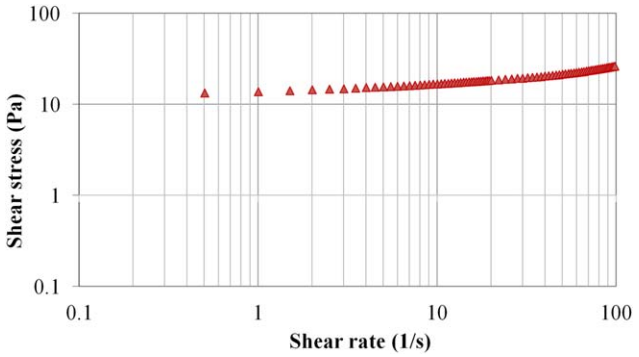

Figure 5. Flow curve of 0.09 wt% Carbopol solution.

[Color figure can be viewed in the online issue, which is available at wileyonlinelibrary.com.]

rheological data can be represented by the Hershel-Bulkley model (Equation 6),[24] with $\tau_0 = 10.8$ Pa, $\kappa = 1.99$ Pa·s, and $n = 0.39$. At higher shear rates, the viscosity of the Carbopol solution reaches a constant value close to 0.1 Pa·s

$$\tau = \pm\tau_0 - k|\dot{\gamma}|^{n-1}(\dot{\gamma}) \tag{6}$$

PIV settings

To determine the flow profiles with the PIV system, two sequential images in a known time interval (Δt) are needed. The best Δt depends on the local velocities of the system. Based on results presented by Gomez et al.,[7] the Δt was calculated from Eq. 7

$$\Delta t = \frac{0.8 Z_l}{U_{tip}} \tag{7}$$

This time frame is such that it avoids particles to travel a distance longer than 25% of the light sheet thickness in the direction normal to the light sheet, before the second snapshot. It has been shown that the maximum velocity close to the impeller can only be a fraction of the U_{tip} (30–50%).[7,25,26]

Two different grids i.e. 55 × 42 and 111 × 85 were used to create the velocity fields. The area of each element of the grid (known as interrogation window) was 4 × 4 mm^2 and 3.85 × 3.85 mm^2, respectively. The sizes of these frames are similar to those used by Torre et al.,[27] Couerbe et al.,[28] and Gomez et al.,[7] where characteristic flow structures were revealed for systems similar to the one used in this study. Each pair of images was processed using the software Flowmanager from Dantec Dynamics. An adaptive correlation, which is based on cross-correlation techniques,[29] was employed to calculate the velocity vectors. This technique reduces the size of the interrogation window progressively to improve the dynamic range and increase the space resolution.[30] For this study, a single refinement step was used and an overlap of 25% between interrogation areas was included in the correlation process.

The number of photos necessary to obtain reliable time-averaged velocities was determined by observing the deviation of the average of sets with 400, 600, 800, 1,000 and 1,200 measurements with respect to a large group of 1,800 measurements, as described by Gomez et al.[7] Thus, the mean velocity vector of a set of 800 pairs of photos was established as a steady time-averaged result for each interrogation window. The trigger presented in the experimental setup section was used to take each pair of photos at the same impeller position (see Figure 2c).

Results and Discussion

Impeller clearance from vertical wall

The flow generated by an A100 impeller at 9.41 s^{-1} is presented in Figure 6. The mean axial-radial circulation can be described as two strong jets coming out from the impeller blades. The flow is recirculated through two main loops; in one loop flow goes toward the low-pressure zone of the impeller, whereas in the other one the flow moves toward the center of the front face of the impeller. In Figure 6, the strong segregation of the flow and the boundary of the active mixing zone are also evident.

The flow fields of the three evaluated clearances are presented in Figure 7. The main differences among the three cases are the discharge angle and the strength of the jets, which significantly affect the size and shape of the active mixing zone. The discharge angle was calculated by averaging the angle with respect to the impeller axis of all the vectors going from right to left at $x^* = 0.35$ (Figure 2c). The discharge angles at $E/D = 0.26$, 0.56 and 0.62, were determined to be 40°, 32° and 30°, respectively. The effect of clearance on the jet strength can be evaluated by examining the velocity at an axial distance away from the impeller. At $x^* = 0.5$ the maximum velocity for the shortest clearance ($E/D = 0.26$) was 29.7% of U_{tip} (tip speed), whereas at $E/D = 0.62$ it was 36.7%.

The effect of clearance is only significant when there is a strong interaction between the active zone and the vessel walls. At 6.93 s^{-1} the cavern does not reach the wall behind the impeller, and the effect of clearance is negligible. As shown in Figure 8a, there is a noticeable similarity among the velocity profiles across a vertical sample line ($x = 7.5$

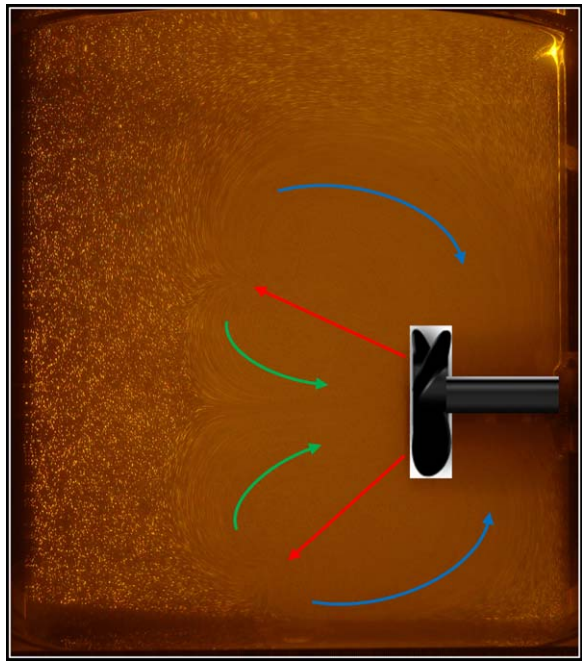

Figure 6. Flow visualization at $Z = 0$, showing the strong jets coming out from the impeller blades (red), the circulating loop going toward the low-pressure zone behind the impeller (blue), and the circulating flow towards the front center of the impeller (green).

[Color figure can be viewed in the online issue, which is available at wileyonlinelibrary.com.]

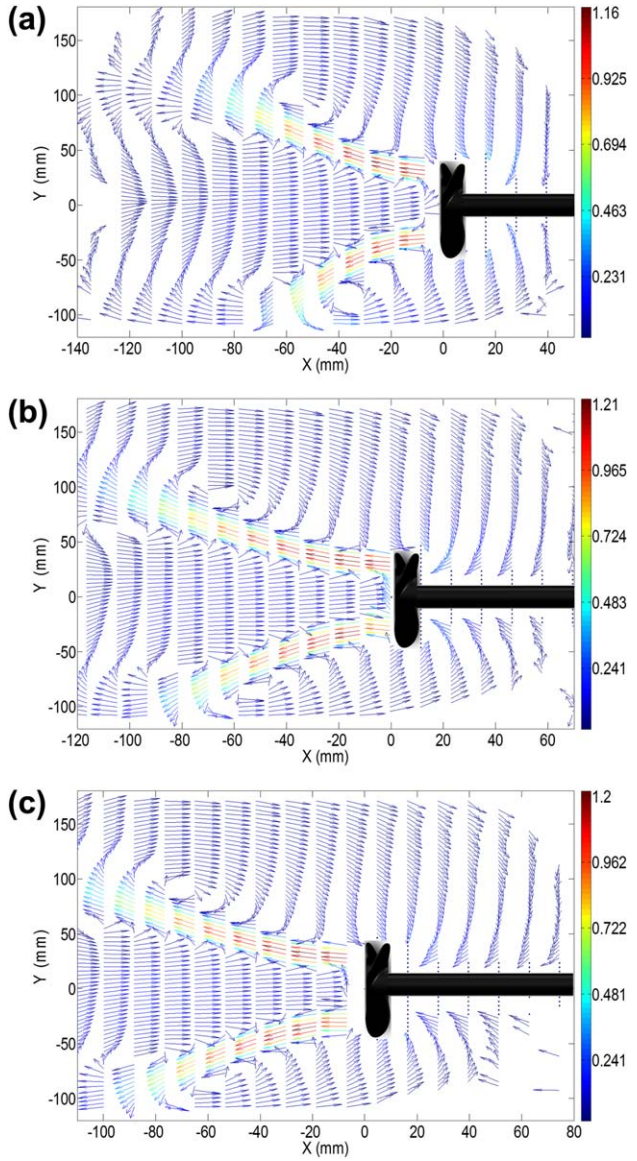

Figure 7. Mean planar velocity fields at $Z = 0$ for (a) $E/D = 0.26$, (b) $E/D = 0.56$, and (c) $E/D = 0.62$.

Velocity vectors colored by velocity magnitude (m/s). [Color figure can be viewed in the online issue, which is available at wileyonlinelibrary.com.]

mm) for the three different clearances. On the other hand, at 11.4 s^{-1} (Figure 8b) there are considerable differences, especially at the height of the impeller discharge ($y^* \approx 0.3$), where the velocity is higher for the two largest clearances. This suggests a positive correlation between clearance and cavern size, and is supported by the velocity distributions in Figure 9. Interdependency between clearance and cavern size has been found by others, e.g., Yackel[5] and Bhole et al.[6]

The probability density functions (PDF) of the velocity magnitude for two vector maps ($Z = 0$ and $Z = 5$) are shown in Figure 9. The PDF is a function that provides the probability of a random variable being within a specific interval when integrated over the same interval. The function is computed from the smallest to the largest values of the variable at the specific plane, using a normal distribution. The probability of values out of the plotted range is equal to zero.

At $E/D = 0.26$ an unfavorable condition arises, since the average velocity is lower compared to the other cases. Another observation is the uneven distribution of velocities for the three clearances, where significant probabilities exist for velocities below 10% of U_{tip}. The high-velocity values at the tail of the distribution correspond to the small fraction of fluid leaving the impeller blades in the axial direction. The lower velocities represent most of the active area, where high-viscosities predominate due to the low-shear rates.

In general, it was found that the cavern volume and the average velocity near the impeller can be enhanced by increasing the clearance from the rear wall. However, this progress curve tends to a maximum, where high values (over 0.56 for the E/D ratio in this case) do not provide significant improvement.

Vessel shape: cylindrical and rectangular

The cylindrical and rectangular vessels showed in Figure 2a and 2b were used to evaluate the effect of vessel shape on the macroscale structures of the flow. Since the shortest clearance accentuates the interaction between vessel walls and cavern, the E/D was set to 0.26 to study such effect. Figure 10 shows velocity fields at $Z = 0$ for the two cases. For the sake of clearness only velocity vectors with magnitudes over 2% of U_{tip} were plotted, showing an approximate cavern size and shape for the two tanks. The flow structures are very similar, but the region occupied by the vectors

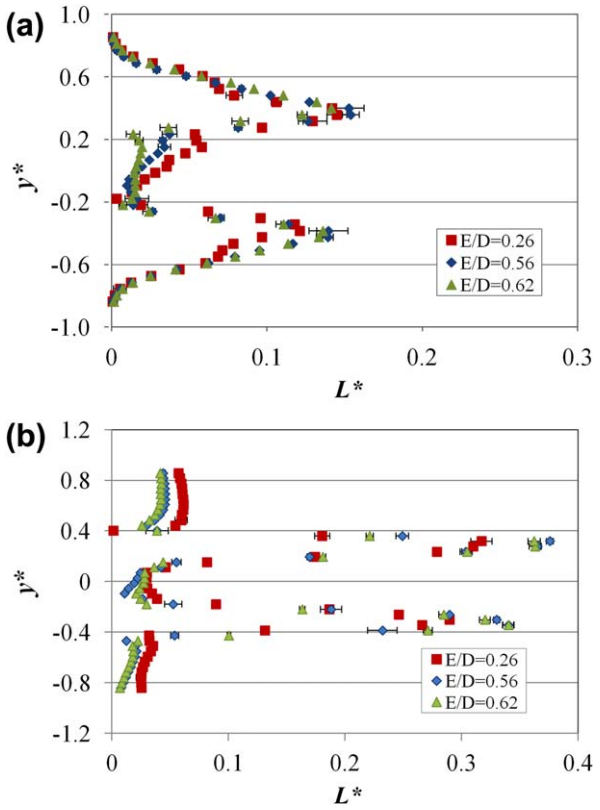

Figure 8. Normalized velocity profiles L^* at $x = 7.5$ mm and plane $Z = 0$ for (a) $N = 6.93$ s^{-1}, and (b) $N = 11.4$ s^{-1}.

The error bars indicate the standard deviation for three measurements. [Color figure can be viewed in the online issue, which is available at wileyonlinelibrary.com.]

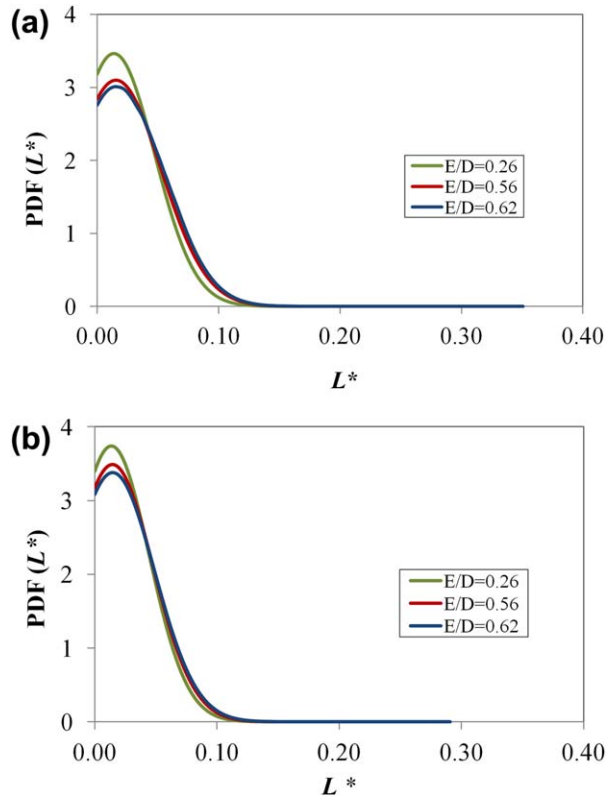

Figure 9. Probability density functions (PDF) of the normalized velocity (L^*), at various clearances on (a) $Z = 0$, and (b) $Z = 5$.

[Color figure can be viewed in the online issue, which is available at wileyonlinelibrary.com.]

corresponding to the rectangular vessels is noticeably larger, especially in the upper part.

A quantitative comparison is presented in Figure 11 for two different impeller velocities. At 5.45 s^{-1} (Figure 11a), the caverns do not touch the vessel wall, resulting in the overlapped velocity profiles. Contrariwise, at 11.4 s^{-1} there are some locations within the cavern with major velocity differences. At the higher angular speed the rectangular vessel offers a peak velocity 18% higher than the velocity of the cylindrical vessel at $y^* \approx 0.7$ (velocity of the jet). Another observation shown in the upper part of the curves is that the

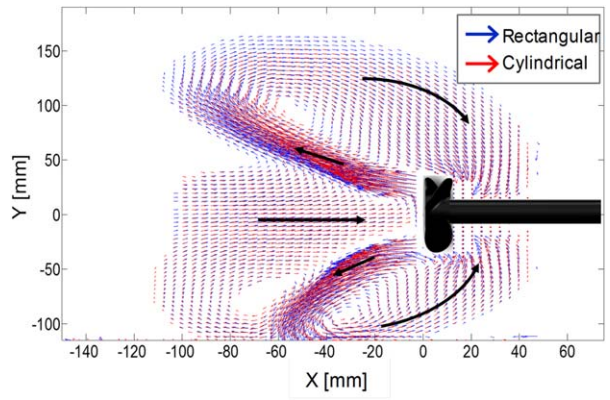

Figure 10. Mean planar velocity fields at 11.4 s^{-1} for $Z = 0$ in rectangular and cylindrical vessels.

[Color figure can be viewed in the online issue, which is available at wileyonlinelibrary.com.]

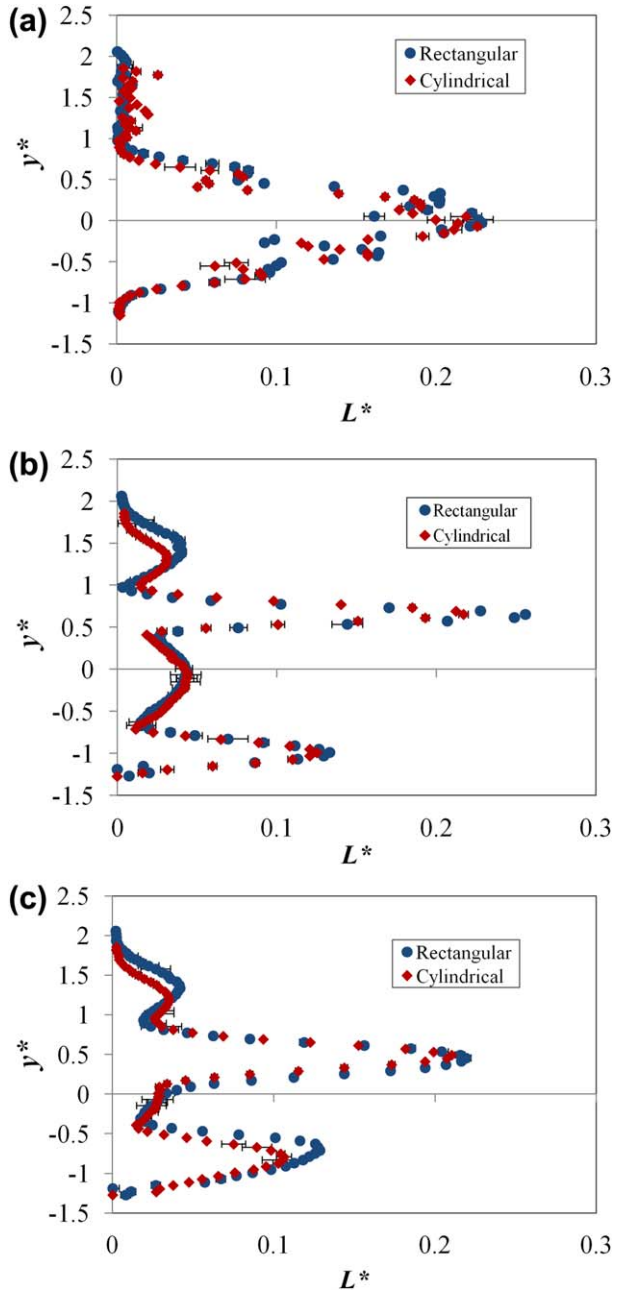

Figure 11. Velocity profiles at $x = 50$ mm for (a) $Z = 0$ and $N = 5.4$ s^{-1}, (b) $Z = 0$ and $N = 11.4$ s^{-1}, and (c) $Z = 5$ and $N = 11.4$ s^{-1}.

[Color figure can be viewed in the online issue, which is available at wileyonlinelibrary.com.]

extent of the motion is larger for the rectangular tank. This statement can be extended to the entire fluid domain, since at $Z = 5$ similar differences can be observed. Thus, a larger cavern size is obtained when mixing takes place in a rectangular tank.

A noticeable characteristic of the velocity profiles at 11.4 s^{-1} (Figure 11b and 11c), is an axi-asymmetric pattern having higher velocities for the upper jet. This reflects how the clearance from the bottom wall of the vessel can restrict the evolution of the flow and the extent of the dynamic zone.

The combined effect of clearance from the rear-wall and vessel shape was assessed by defining a margin velocity. Although this limit is not the actual boundary between the

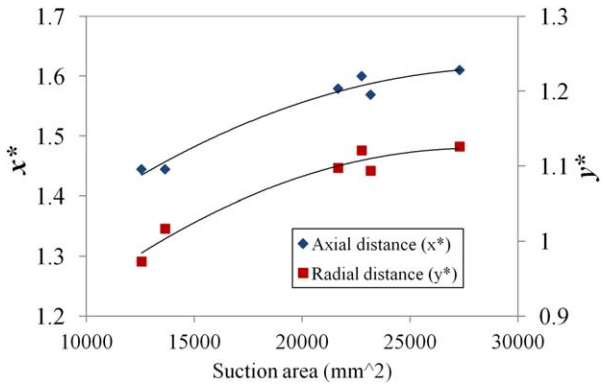

Figure 12. Cavern extent vs. suction area.

[Color figure can be viewed in the online issue, which is available at wileyonlinelibrary.com.]

cavern and the dead zone, it provides a baseline to compare the extent of the cavern under different suction areas. The boundary velocity was set following the approach presented in Adams and Barigou,[22] where 1% of the U_{tip} is assumed to indicate the limit of the pseudo-cavern. The distance from impeller center to this limiting boundary was measured in the plane $Z = 0$. This was done for both axial and radial directions, under different combinations of clearance and vessel shape. The suction area was calculated as πDI, where D is the impeller diameter and I is the length from impeller tip to rear-wall. The results, presented in Figure 12, show a clear trend where the cavern volume increases with enlarging the suction area (x^* and y^* show the extent of the cavern in the axial and radial directions, respectively). At small suction areas, there is a considerable restriction of the flow to the suction zone behind the impeller. The restriction constrains the contribution of the inertial forces and consequently the extent of the cavern. To attain a certain flow pattern, this decrease of inertial forces may be compensated with higher rotational speeds, which will in turn increase the power consumption. The relationship between cavern size and suction area is not linear and tends to reach an asymptote that is related to the maximum pumping capacity of the impeller. Above 22,000 mm^2 the cavern growth is not significant and the E/D ratio for this suction area ($E/D \approx 0.5$) agrees with optimum E/D ratios presented in literature for mixing of pulp suspensions with side entry impellers.[5,6,31]

Impeller Geometry

Measurements were carried out for three axial flow impellers with different blade angles. The Yield-stress-Reynolds number ($Re_y = \rho N^2 D^2/\tau_y$) was used to characterize the impeller performance. This definition of Reynolds number has been used in other studies to characterize impeller and mixing performance.[3,32] The velocity distributions for each impeller are presented in Figure 13. The N_p vs. Re_y and N_q vs. Re_y curves are presented in Figure 17.

The flow-structures generated by the three impellers (at 11.4 s^{-1}) show significant differences. The effect of the pitch ratio (0.44, 0.9 and 1.5 for the Maxflo, A312 and A100, respectively) is reflected on the discharge angle and jet size and shape, which define the characteristics of the cavern. Thus, for the Maxflo, a weak jet with a high discharge angle with respect to the axis produces a small cavern with a toroidal shape around the impeller. Characteristics of the A312 and A100 flow include bigger cavern size and smaller discharge angles, which allow the cavern to grow in the axial direction. This flow pattern generates a kidney-like shape cavern and induces a reversed flow toward the center of the front face of the impeller.

The location of the highest velocity at $Z = 0$ is for all cases $y \approx 30$ mm and $x \approx 5$ mm. However, the magnitudes differ considerably between one another. The velocities are 15, 23 and 35% of the U_{tip} for the Maxflo, A312 and A100, respectively. Similar low velocity conditions have been reported in other studies.[2,7]

The differences in the three flow patterns are reflected not only at $Z = 0$, but also at $Z = 5$ (Figure 13b), where higher velocities and stronger axial discharge are observed for the A100. At $Z = 5$, the strong tangential flow for the Maxflo, implies that part of the fluid is being dragged around the impeller in concentric lines as it rotates. On the other hand, the axial components of the velocity for the A312 and particularly for the A100 become more significant in the velocity map. These differences are related to the angle of attack of each impeller, which is described by the pitch ratio. The highest pitch ratio of the A100 impeller implies the highest angle of attack. This characteristic allows the blade to disrupt the closed streamlines produced by the viscous forces and imparts momentum in the axial direction more effectively. Additionally, lower viscous forces are expected in the discharge zone of the A100, since the shear rate in the

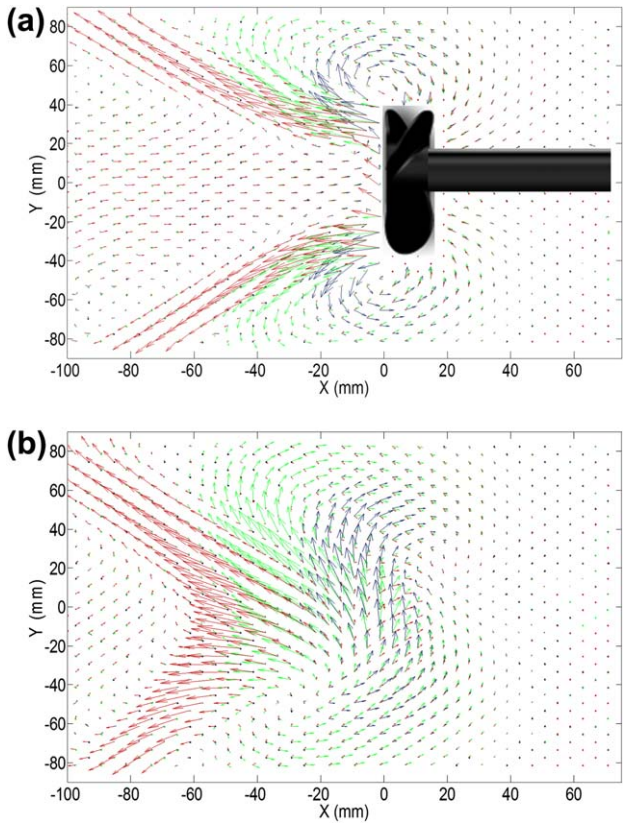

Figure 13. Average velocity fields at 11.4 s^{-1} for three different impellers.

Blue vectors correspond to the Maxflo Mark II, green vectors correspond to the A312 and red vectors correspond to the A100 at (a) $Z = 0$, and (b) $Z = 5$. [Color figure can be viewed in the online issue, which is available at wileyonlinelibrary.com.]

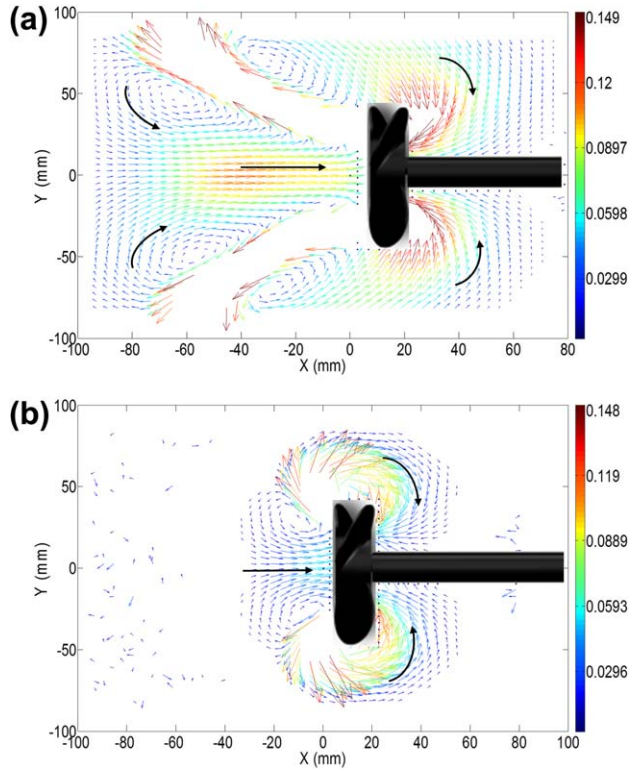

Figure 14. Mean planar velocity fields at 9.41 s^{-1} in $Z = 0$ for (a) A100 impeller, and (b) Maxflo Mark II impeller.

Velocity vectors colored by velocity magnitude (m/s). [Color figure can be viewed in the online issue, which is available at wileyonlinelibrary.com.]

vicinity of this impeller is higher compared to the Maxflo and A312 impellers.[2]

Figure 14 shows the velocity vectors with magnitudes above 1×10^{-3} and below 0.14 m/s to better show the flow characteristics. In Figure 14a the strong discharge of the A100 produces regions with large vorticity and perhaps higher shear rates due to the high-velocity gradients in the vicinity of the jets (located on the white spaces). Moreover, the interaction between the discharge flow and the streams going back to the suction areas in front of and behind the impeller, create small circulations loops at the inner and outer side of the jet.

It is believed that those circulation loops are segregated zones from the bulk flow, since high concentrations of dye (Rhodamine B) are observed at those positions without significant change over time (Figure 15). As the discharge angle decreases (higher angular speed), the small circulation loops move away from the impeller in the axial and radial direction and the reversed volumetric flow coming through the center becomes prominent. For the Maxlfo (Figure 14b), the quasi-radial discharge drives most of the fluid to the low-pressure zone of the impeller through one main circulation loop. Due to the short extent of the jets, the additional circulation loop at the outer side of the jet observed for the A100 merges with the suction stream behind the impeller. In this figure the small-toroidal active zone is evident for the Maxflo, whereas the cavern limit for the A100 impeller is outside of the area covered by the PIV photos.

A quantitative comparison of the axial-radial flow generated by the three impellers is exposed in Figure 16. The figure shows the probability density function (PDF) of the velocity magnitudes in the "x" and "y" directions on the plane $Z = 0$ for each impeller. The predominant axial flow for the A100 is reflected by the wider distribution of U^* and the lower probability of velocities close to zero (Figure 16a). Figure 16b shows that the increase in axial flow occurs without losing the radial component of the velocity; hence, the cavern grows in both directions.

The power and pumping number vs. Yield-stress-Reynolds number curves (Figure 17) confirms the laminar-transitional

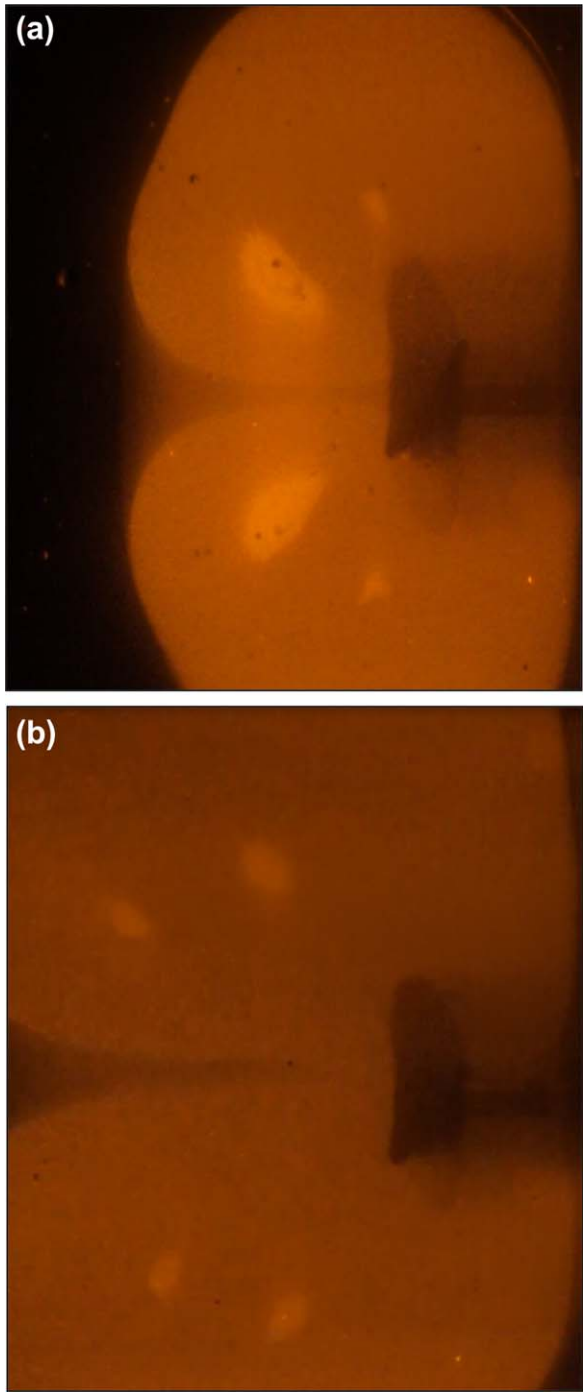

Figure 15. Photography of segregated circulation loops at (a) 5.4 s^{-1}, and (b) 6.93 s^{-1}.

[Color figure can be viewed in the online issue, which is available at wileyonlinelibrary.com.]

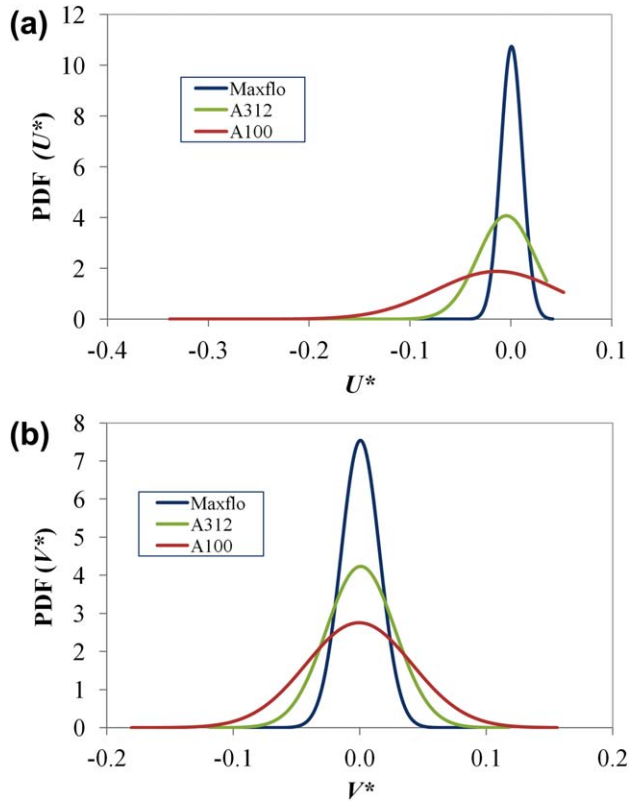

Figure 16. Probability density function on the plane $Z = 0$ of (a) normalized x-component of velocity, and (b) Normalized y component of velocity.

[Color figure can be viewed in the online issue, which is available at wileyonlinelibrary.com.]

flow regime and the prevailing axial discharge (Figure 17b) of the A100 impeller. The pumping capacity was defined as the volumetric flow rate passing through a circular plane with the same radius and center as the impeller, placed 7 mm in front of the impeller. Based on the velocity symmetry shown in Figure 13, the velocity profile (from $y^* = 0$ to $y^* = 0.5$) of the mean velocity normal to the surface was used to integrate the flow area.[33]

Overall the results indicate that a higher pitch ratio provides bigger cavern size and improves mixing performance when axial flow is desired. Although the power requirements for the low-pitch ratio are lower, the required mixing mechanisms in the laminar regime can be negatively affected by the lack of perturbation of the streamlines created by viscous forces.

Computational modeling of flow patterns

Computational fluid dynamics (CFD) model of the studied systems was developed to evaluate the potential of computational codes to predict flow behavior and mixing characteristics for any scale and geometry. The model solves the continuity and momentum equations along with a rheological equation (Eq. 6) using ANSYS Fluent. The computational domain resembles all the main geometrical characteristic of the system used during the experimental work. A complete description of the meshing process, solution strategy and boundary conditions can be found elsewhere.[34]

The results obtained from the PIV experiments were used to evaluate the model predictions of velocity vectors and large-scale flow patterns at different locations inside the mixer. Figure 18 shows a computed velocity field at $Z = 0$ using the A100 impeller. These flow patterns reflect distinctive flow properties observed in PIV flow visualization experiments (Figure 7).

The adequate prediction of the impeller discharge is confirmed by the extension and direction of the jets coming out from the blades. As observed in Figures 7b and 18 (same operating conditions), the extent of the lower part of the impeller discharge reaches approximately 70 mm in the X-axis and 110 mm in the Y-axis, where the fluid is forced to flow back to the low pressure zone by the bottom wall of the tank. Likewise, the computed flow in the lower part clearly displays the recirculation loops (at $X = -40$, $Y = -90$ and $X = -90$, $Y = -80$) redirecting the flow to the suction zones. The prediction of flow properties above the impeller shaft is not as good as the lower part, likely due to simplifications in the approach (multiple reference frame) used to model the impeller rotation.[34] The deviation of the computed velocity vectors decreases at locations closer to the impeller as shown by the velocity profile in Figure 19. The predicted velocities on a plane $Z = 0$ were plotted for a sample line located at $X = 7.5$ mm. The values measured over the same sample line during the PIV experiments (identical operating conditions) are shown in Figure 8b. There is a satisfactory agreement on the velocity values and the peak locations above and below the impeller shaft.

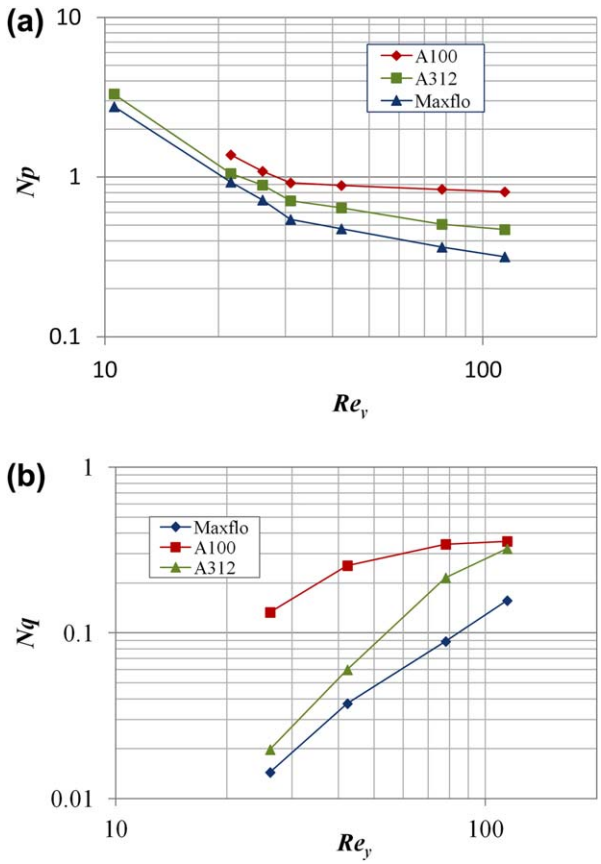

Figure 17. (a) Pumping number vs yield stress Reynolds number, and (b) power number vs. yield stress Reynolds number.

[Color figure can be viewed in the online issue, which is available at wileyonlinelibrary.com.]

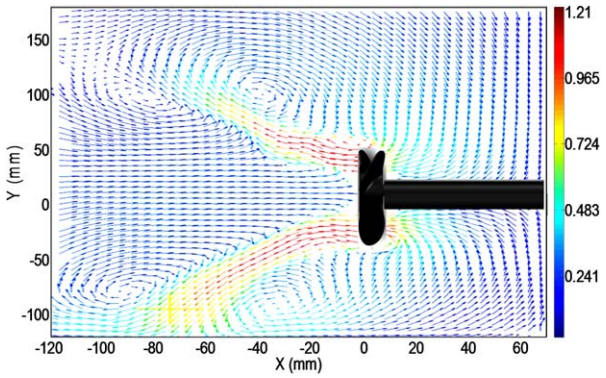

Figure 18. Two dimensional (2-D) velocity field at Z = 0 generated by the A100 impeller at 11.4 s^{-1}.

[Color figure can be viewed in the online issue, which is available at wileyonlinelibrary.com.]

To further evaluate the capabilities and limitations of the developed CFD model, the computed flow patterns for different impellers were compared with PIV flow visualization experiments. Figure 20 confirms that the CFD model can predict the effect of the impeller blade design on the discharge jet structure and other active zones properties. The flow generated by the A100 impeller (Figure 20a) has a stronger axial flow and larger areas displaying high velocities compared to the flow obtained with the A312 impeller (Figure 20b). The discharge angle at $x^* = 0.35$ is 34° (in agreement with experimental results presented in a previous section) and 44° for A100 and A312, respectively. These results confirmed the experimentally observed effect of the pitch ratio on the axial/radial discharge of a specific impeller, where larger pitch ratios tend to create stronger axial flows.

Overall, the model was able to predict the main features of the flow mixing with different impellers at a range of operating conditions. Hence, it can be stated that important flow field variables like discharge angles, segregated zones, circulation loops, velocity distributions, shear rate levels among others, can be obtained at any scale by solving fundamental equations of momentum, mass and energy (if required) conservation along with a solid representation of fluid rheology and geometry of the system.

At larger scales, flow patterns with characteristics similar to the ones described in this study are expected for comparable Reynolds numbers. Based on the experimental flow visualization and computational flow modeling, suggestions may be made for the design of larger scale mixers. For larger impeller diameters, larger clearance from the rear walls is required to prevent flow restrictions to the suction zone behind the impeller, thereby maximizing the impeller pumping capacity. Likewise, the distance from the impeller to the wall of the bottom of the tank needs to be increased to not force the jet coming from the blades toward the back of the impeller, before reaching its maximum discharge range in the axial direction.

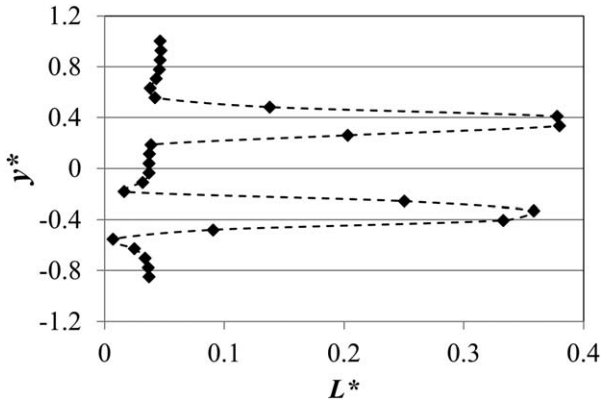

Figure 19. Computed velocity profile (L^*) on plane Z = 0 at N = 11.4 s^{-1} over sample line at x = 7.5 mm.

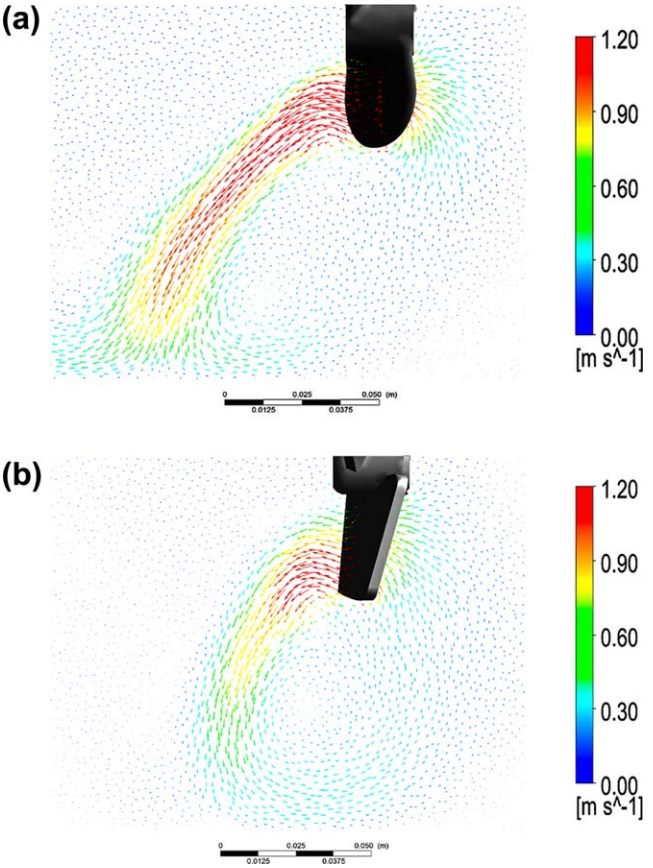

Figure 20. Computed planar velocity fields at 11.4 s^{-1} in Z = 0 for (a) A100 impeller, and (b) A312 impeller.

Velocity vectors colored by velocity magnitude (m/s). [Color figure can be viewed in the online issue, which is available at wileyonlinelibrary.com.]

Conclusions

The effects of clearance, vessel shape, and impeller type in mixing tanks equipped with side-entry impellers on the hydrodynamics of a non-Newtonian model fluid (0.09 w/w % Carbopol solution) were evaluated using particle image velocimetry. The different flow structures revealed that the ratio of inertial and viscous forces largely defines the flow pattern. Due to the shear thinning behavior of a non-Newtonian fluid, the viscous forces are very sensitive to the shear rate distribution of each mixing configuration. High-pitch ratios improve the impeller discharge, thereby providing a dominantly axial flow and a larger mixing volume. In the same manner, the suction area defined by the clearance and vessel shape, determines the inertia on the flow ejected by the impeller. By this principle it conditions the extent of the cavern in the axial and radial directions. Under some particular conditions, new circulation loops arise in the flow pattern. These zones are closed tubes segregated from the

main circulation loop and their locations depend on the Reynolds number. At a specific rotational speed, the largest cavern size and highest pumping capacity correspond to the impeller with the highest power number.

Notation

D = impeller diameter, cm
E = impeller clearance from the side wall, cm
F_A = axial thrust, N
H = liquid level, cm
k = consistency index, Pa·s
K_s = Metzner and Otto impeller constant
l = mixing vessel length, cm
L_b = vane length, m
L = total velocity, m/s
L^* = normalized total velocity, L/U_{tip}
M = torque, N·M
n = flow index
N = rotational speed, s^{-1}
N_p = power number
N_q = pumping number
N_f = axial force number
P = power, W
Q = flow rate, m^3/s
R_b = vane radius, m
Re_y = yield stress Reynolds number, Pa
T = diameter of cylindrical tank, cm
U_{tip} = tip speed, m/s
U = axial velocity, m/s
U^* = normalized axial velocity, U/U_{tip}
V = vertical velocity, m/s
V^* = normalized vertical velocity, V/U_{tip}
W = mixing vessel width, cm
x = axial distance in front of the impeller, mm
x^* = x/D
y = vertical distance from impeller center, mm
y^* = y/D
Z = radial position from the impeller center, cm
Z_l = laser sheet thickness, mm

Greek letters

ρ = fluid density, kg/m^3
Ω = Angular velocity, rad/s
τ = shear stress, Pa
$\dot{\gamma}$ = shear rate, s^{-1}
τ_y = yield stress, Pa

Literature Cited

1. Kelly W, Gigas B. Using CFD to predict the behavior of power law fluids near axial flow impellers operating in the transitional flow regime. *Chem Eng Sci*. 2003;58(10): 2141–2152.
2. Kumaresan T, Joshi J. Effect of impeller design on the flow pattern and mixing in stirred tanks. *Chem Eng J*. 2006;115(3):173–193.
3. Bhole MR, Bennington CPJ. Performance of four axial flow impellers for agitation of pulp suspensions in a laboratory-scale cylindrical stock chest. *Ind Eng Chem Res*. 2010;49(9):4444–4451.
4. Hemrajani RR, Tatterson GB. *Mechanically Stirred Vessels*. In: Paul EL, Atiemo-Obeng VA, Kresta SM, eds. *Handbook of Industrial Mixing*. Hoboken, NJ: Wiley-Interscience; 2004.
5. Yackel DC. *Pulp and Paper Agitation: The History, Mechanics, and Process*. Atlanta, GA: TAPPI Press; 1990.
6. Bhole MR, Hui LK, Gomez C, Bennington CPJ, Dumont GA. The Effect of off-wall clearance of a side-entering impeller on the mixing of pulp suspensions in a cylindrical stock chest. *Can J Chem Eng*. 2011;9999:1–11.
7. Gomez C, Bennington CPJ, Taghipour F. Investigation of the flow field in a rectangular vessel equipped with a side-entering agitator. *J Fluids Eng*. 2010;132(5):1–13.
8. Adrian R. Particle-Imaging techniques for experimental fluid-mechanics. *Annu Rev Fluid Mech*. 1991;23(1):261–304.
9. Prasad AK. Particle image velocimetry. *Curr Sci*. 2000;79(1):51–60.
10. Mckenna SP, Mcgillis WR. Performance of digital image velocimetry processing techniques. *Exp Fluids*. 2002;32:106–115.
11. Curran SJ, Hayes RE, Afacan A, Williams MC, Tanguy P. Properties of carbopol solutions as models for yield-stress fluids. *J Food Sci*. 2002;67(1):176–180.
12. Piau JM. Carbopol gels: elastoviscoplastic and slippery glasses made of individual swollen sponges meso- and macroscopic properties, constitutive equations and scaling laws. *J Non-Newtonian Fluid Mech*. 2007;144(1):1–29.
13. Carnali JO, Naser MS. The use of dilute solution viscometry to characterize the network properties of carbopol microgels. *Colloid Polym Sci*. 1992;270:183–193.
14. Roberts GP, Barnes HA. New measurements of the flow-curves for carbopol dispersions without slip artefacts. *Rheologica Acta*. 2001; 40(5):499–503.
15. Gomez C, Derakhshandeh B, Hatzikiriakos SG, Bennington CPJ. Carbopol as a model fluid for studying mixing of pulp fibre suspensions. *Chem Eng Sci*. 2010;65(3):1288–1295.
16. Arratia PE, Kukura J, Lacombe J, Muzzio FJ. Mixing of shear-thinning fluids with yield stress in stirred tanks. *AIChE J*. 2006;52: 2310–2322.
17. Hu Y, Liu Z, Yang J, Jin Y, Cheng Y. Study on the reactive mixing process in an unbaffled stirred tank using planar laser-induced fluorescence (PLIF) technique. *Chem Eng Sci*. 2010;65:4511–4518.
18. Magnin A, Piau JM. Cone-and-plate rheometry study of yield stress fluids. *Study of an aqueous gel*. *J Non-Newtonian Fluid Mech*. 1990; 36:85–108.
19. Steffe JF. *Rheological Methods in Food Process Engineering*. 2nd ed. East Lansing, MI: Freeman Press; 1996:158–250.
20. Barnes HA. Nguyen QD. Rotating vane rheometry – a review. *Science*. 2001;98:1–14.
21. Metzner AB, Otto RE. Agitation of non-newtonian fluids. *AIChE J*. 1957;3:3–10.
22. Adams LW, Barigou M. CFD Analysis of caverns and pseudo-caverns developed during mixing of non-newtonian fluids. *Chem Eng Res Des*. 2007;85(5):598–604.
23. Chhabra RP, Richardson JF. *Non-Newtonian Flow and Applied Rheology*. 2nd ed. Burlington, MA: Elsevier; 2008.
24. Kalyon DM. Apparent slip and viscoplasticity of concentrated suspensions. *J Rheol*. 2005;49(3):621–640.
25. Zalc JM, Alvarez MM, Muzzio FJ, Arik BE. Extensive validation of computed laminar flow in a stirred tank with three rushton turbines. *AIChE J*. 2001;47(10):2144–2154.
26. Bugay S, Escudié R, Liné A. Experimental analysis of hydrodynamics in axially agitated tank. *AIChE J*. 2002;48(3):463–475.
27. Torre J, Fletcher D, Lasuye T, Xuereb C. Single and multiphase CFD approaches for modelling partially baffled stirred vessels: comparison of experimental data with numerical predictions. *Chem Eng Sci*. 2007;62(22):6246–6262.
28. Couerbe G, Fletcher D, Xuereb C, Poux M. Impact of thixotropy on flow patterns induced in a stirred tank: numerical and experimental studies. *Chem Eng Res Des*. 2008;86(6):545–553.
29. Keane RD, Adrian RJ. Theory of cross-correlation analysis of PIV images. *Appl Sci Res*. 1992;49:191–215.
30. Scarano F, Riethmuller ML. Iterative multigrid approach in piv image processing with discrete window offset. *Exp Fluids*. 1999; 26(6):513–523.
31. Reed CS. Selecting the right equipment for agitation and blending. Part 3. *Tappi J*. 1995:248–250.
32. Pakzad L, Ein-mozaffari F, Chan P. Analysis of cavern formation in mixing of yield stress fluids using tomography and CFD modeling. *Sixth International Symposium on Mixing in Industrial Process Industries* – ISMIP VI; 2008:1–2.
33. Jaworski Z, Nienow AW, Dyster KN, An LDA Study of the turbulent flow field in a baffled vessel. *Can J Chem Eng*. 1996;74:3–15.
34. Sossa J. *Experimental and Computational Study of Mixing Behavior in Stirred Tanks Equipped with Side-Entry Impellers* [Thesis]. University of British Columbia. Vancouver, BC; 2012.

Manuscript received Apr. 14, 2013, and revision received Oct. 4, 2013.